Three-Dimensional Segmentation and Quantitative Measurement of the Aqueous Outflow System of Intact Mouse Eyes Based on Spectral Two-Photon Microscopy Techniques

Xianzeng Zhang,[1,2] Nenrong Liu,[1,3] Peng Un Mak,[4] Sio Hang Pun,[5] Mang I. Vai,[4] Omid Masihzadeh,[6] Malik Y. Kahook,[6] Tim C. Lei,[1] and David A. Ammar[6]

[1]Department of Electrical Engineering, University of Colorado, Denver, Colorado, United States
[2]College of Photonic and Electronic Engineering, Fujian Normal University, Fuzhou, China
[3]College of Physics and Energy, Fujian Normal University, Fuzhou, China
[4]Department of Electrical and Computer Engineering, University of Macau, Macau, China
[5]State Key Laboratory of Analog and Mixed Signal VLSI, University of Macau, Macau, China
[6]Department of Ophthalmology, University of Colorado Denver, Colorado, United States

Correspondence: David A. Ammar, Department of Ophthalmology, University of Colorado School of Medicine, 12800 E. 19th Avenue, MS 8311, RC-1 North Room #5105, Aurora, CO 80045, USA; david.ammar@ucdenver.edu.

Submitted: October 23, 2015
Accepted: March 16, 2016

Citation: Zhang X, Liu N, Mak PU, et al. Three-dimensional segmentation and quantitative measurement of the aqueous outflow system of intact mouse eyes based on spectral two-photon microscopy techniques. *Invest Ophthalmol Vis Sci*. 2016;57:3159–3167. DOI:10.1167/iovs.15-18491

Purpose. To visualize and quantify the three-dimensional (3D) spatial relationships of the structures of the aqueous outflow system (AOS) within intact enucleated mouse eyes using spectral two-photon microscopy (TPM) techniques.

Methods. Spectral TPM, including two-photon autofluorescence (TPAF) and second-harmonic generation (SHG), were used to image the small structures of the AOS within the limbal region of freshly enucleated mouse eyes. Long infrared excitation wavelengths (930 nm) were used to reduce optical scattering and autofluorescent background. Image stacks were collected for 3D image rendering and structural segmentation. For anatomical reference, vascular perfusion with fluorescent-conjugated dextran (150 KDa) and trans-corneal perfusion with 0.1 μm fluorescent polystyrene beads were separately performed to identify the episcleral veins (EV) and the trabecular meshwork (TM) and Schlemm's canal (SC), respectively.

Results. Three-dimensional rendering and segmentation of spectral two-photon images revealed detailed structures of the AOS, including SC, collector channels (CC), and aqueous veins (AV). The collagen of the TM was detected proximal to SC. The long and short axes of the SC were 82.2 ± 22.2 μm and 6.7 ± 1.4 μm. The diameters of the CC averaged 25.6 ± 7.9 μm where they originated from the SC (ostia), enlarged to 34.1 ± 13.1 μm at the midpoint, and narrowed to 18.3 ± 4.8 μm at the junction of the AV. The diameter of the AV averaged 12.5 ± 3.4 μm.

Conclusions. Spectral TPM can be used to reconstruct and measure the spatial relationships of both large and small AOS structures, which will allow for better understanding of distal aqueous outflow dynamics.

Keywords: second-harmonic generation, two-photon fluorescence microscopy, nonlinear microscopy, glaucoma, aqueous outflow

Aqueous humor exits the eye through the conventional aqueous outflow system (AOS), passing through the trabecular meshwork (TM), Schlemm's canal (SC), collector channels (CC), and aqueous veins (AV) before eventually terminating at episcleral veins (EV) or the surface of the eye. It is hypothesized that structural abnormalities or functional changes in either the juxtacanalicular TM or SC lead to elevated IOP and the eventual development and progression of primary open-angle glaucoma (POAG).[1] The ability to visualize the detailed structure of the AOS (especially the SC and TM) at high resolution to obtain reproducible structural measurements would be of great potential value for early detection of glaucoma and could improve clinical interventions.[2,3] Currently available imaging techniques, including ultrasound biomicroscopy,[4,5] optical coherence tomography (OCT),[6,7] and three-dimensional (3D) micro–computed tomography,[8] have greatly influenced the standards of clinical and surgical ophthalmic care, not only to detect the disease but also to follow its progress. However, the aforementioned imaging modalities can only detect disease changes associated with nerve and retina damage and are unable to diagnose the earliest stages of POAG. Moreover, they are largely unable to elucidate the functional state of ocular tissues.

Two-photon microscopy (TPM) has found increasing use in laboratory-based biomedical imaging due to its subcellular resolution and its ability to obtain structural and functional information.[9] In two-photon autofluorescence (TPAF), two photons interact simultaneously at the focal point to excite an endogenous biomolecular chromophore to generate a blue-shifted fluorescent photon.[10,11] Another two-photon nonlinear

Investigative Ophthalmology & Visual Science

process is second-harmonic generation (SHG), which occurs only when photons interact with noncentrosymmetric macromolecular structures, such as collagen fibers. Collagen fibers can simultaneously "scatter" and "combine" two infrared photons to generate a new second-harmonic photon (with twice the energy of the original photons).[12] In typical TPM, both TPAF and SHG are generated by a single-femtosecond pulsed laser in the infrared wavelength, and the two signals can be spectrally separated using a spectrometer or a dichroic mirror and filter set. Not only can TPM obtain detailed subcellular structures in intact biological tissues without the need for extrinsic dyes and tissue fixation, the use of infrared wavelengths allows for deeper penetration with reduced absorption and scattering, which is particularly important when imaging through the opaque scleral tissue.

Our previous studies have evaluated the usefulness of TPM for imaging the TM and proximal outflow structures of human, pig, and mouse eyes.[13–16] In the present work, we obtained higher resolution images of the SC, CC, and AV within intact enucleated fresh mouse eyes through several technical improvements. The excitation wavelength was tuned to a longer infrared wavelength (930 nm) instead of 800 nm used in our previous work so as to minimize optical scattering of the scleral tissue and to reduce autofluorescence from melanin. This resulted in images of the entire AOS cross-section with greatly improved image quality. Instead of using a broad autofluorescence filter to capture all TPAF signals, the 32 channels of a spectral photomultiplier were used to differentiate individual autofluorescence signals; for example, the melanin within the iris has a broad fluorescent spectrum that can readily be separated from other structures that have a narrower autofluorescent spectrum. With the improved signal-to-noise ratio of these images, segmentation techniques can be applied to separate the different components of the AOS, including the TM, SC, CC, and AV, and to quantify the spatial relationship of the entire outflow pathway in 3D. Our findings provide the foundation for future in vivo animal ophthalmic imaging that would allow for studying the structural changes of the AOS during progression of glaucoma, with the potential to evaluate therapeutic treatments.

Methods

Animal Tissue

All animal research was conducted in compliance with the ARVO Statement for the Use of Animals in Ophthalmic and Vision Research. All animal work was approved by the Institutional Animal Care and Use Committee at the University of Colorado Anschutz Medical Campus (Aurora, CO, USA). Experiments were performed using eyes from adult mice (age 12–20 weeks) of either sex (C57BL/6; Jackson Labs, Bar Harbor, ME, USA). Mice were euthanized by carbon dioxide inhalation followed by cervical dislocation, and eyes were immediately enucleated for imaging. In some experiments, euthanized mice were perfused through the heart with PBS (Life Technologies, Grand Island, NY, USA) containing 1 mg/mL fluorescein isothiocyanate (FITC)-labeled dextran (molecular weight 150 kDa; Sigma-Aldrich Corp., St. Louis, MO, USA) just before enucleation.

Imaging

Two-photon microscopy imaging was performed at the University of Colorado Anschutz Medical Campus Advance Light Microscopy Core using an adapted laser scanning inverted confocal microscope (Zeiss LSM 780; Carl Zeiss AG, Oberkochen, Germany) with a ×40X/1.2NA water-immersion objective. The excitation beam (930 nm) was provided by a mode-locked Ti:Sapphire laser (Spectra-Physics, Irvine, CA, USA) emitting approximately 140 fs width pulses at an 80-MHz repetition rate. The Zeiss inverted microscope was configured in the descanned mode to capture the fluorescent signals using a QUASAR detector (Carl Zeiss AG). This detector has a 32-channel gallium arsenide phosphide (GaAsP) linear photomultiplier tube (PMT) coupled to a prism. The prism disperses the entire range of the emission spectrum (410 to 695 nm) onto the 32-channel PMT. Each channel simultaneously collects a discreet range of optical frequency (~8.9 nm) without the need for multiple emission filters. Using the native software (Zen 2012 Black; Carl Zeiss AG), each spectral channel is pseudo-colored with a unique color ranging from violet to deep red. This allows for emission from all 32 channels to be simultaneously recombined to form a "full-color" image to assist with analysis of the raw data.

When examining the pseudo-colored raw data using this full-color mode, it is apparent that certain molecules with different nonlinear emission spectra can be identified. For instance, the SHG signal from collagen is generated at approximately 465 nm, which is pseudo-colored "blue." In contrast, melanin emits a very broad fluorescent signal covering the spectral range from 490 to 690 nm, and the combination of these multiple pseudo-colored emission channels appears "reddish" in the full-color images. In perfusion experiments, most of the emission spectrum for the yellow fluorescent polystyrene beads was contained in channels corresponding to 539 to 619 nm and appears as "yellow" in the full-color images. Finally, the emission spectrum for the FITC-conjugated dextran was contained in channels corresponding to 513 to 530 nm and appears as "dark green." Using this technique, the fluorescence from these different types of biomolecules/fluorophores can be separated even when the emission spectra of these molecules are somewhat overlapped (Supplementary Methods S1).

Enucleated mouse eyes were placed on a custom-built eye-holder to ensure the anterior/posterior axis of each eye was always kept perpendicular to the imaging axis, yielding transverse cross-sectional images of the eye. The eye-holder was filled with PBS to prevent the tissue from drying during the course of the experiment. To compensate for laser intensity reduction due to tissue scattering while scanning deep into the tissue, a spline extrapolation algorithm was used to increase the laser intensity to obtain uniform signal intensity across the entire scan. The laser power on the sample varied from 0.8 milli-Watt (mW) at the surface to 1.8 mW at the deepest point within the tissue sample, and the pixel dwell time was 1.54 µs. The American National Standards Institute power limit for tissue damage calculated from the parameters of the excitation laser using this pixel dwell time is approximately 57 mW according to Delori et al.,[17] which is an order of magnitude higher than the power used in this study.

Mouse Eye Perfusion

In some experiments, the anterior chambers of enucleated eyes were perfused with a 0.1% (vol/vol) solution of 0.1 µm yellow fluorescent polystyrene beads (λ_{ex} ~575 nm; λ_{em} ~610 nm; 10% solids, Sigma-Aldrich Corp.) in PBS. Perfusions were performed using a programmable motorized syringe pump (Harvard Apparatus, Holliston, MA, USA) fitted with a 10-µL glass micro-syringe (Hamilton, Reno, NV, USA). The Hamilton syringe was connected to a needle made from borosilicate glass tubing (outer diameter, 1.0 mm; inner diameter 0.58 mm; KwikFil; WPI, Sarasota, FL, USA). The tip of the glass micro-

Investigative Ophthalmology & Visual Science

needle was prepared using a pipette puller (Zeitz Instruments GmbH, Martinsried, Germany) and the processed tips had an outer diameter of approximately 3 μm. The tip of the microneedle was inserted manually into the cornea, and PBS containing florescent beads was perfused for 10 minutes at a rate of approximately 0.1 μL/min before imaging.

Image Analysis, Segmentation, and 3D Rendering

Acquired TPM images from a total of eight different eyes were postprocessed using both the microscope control software (Zen 2012 black edition; Carl Zeiss AG) and ImageJ software (http://imagej.nih.gov/ij/; provided in the public domain by the National Institutes of Health, Bethesda, MD, USA). Image postprocessing included brightness and contrast adjustments and single-plane projections of z-stack images. The SHG signal from the tissue collagen defined the corneal and scleral regions of the mouse eye, and a slight indentation of these two regions defined the limbal region. Areas within the limbal region lacking SHG signal were considered as potential fluid-filled AOS (details below). These fluid-filled areas were processed by image segmentation techniques to extract the detail of the large and small structures of the limbus (SC, CC, and AV). The Seg3D software package (University of Utah Center for Integrative Biomedical Computing, Salt Lake City, UT, USA; http://www.sci.utah.edu/cibc-software/seg3d.html) was used for the segmentation processing. In brief, the SHG collagen signal of the images was first down-converted to a monochromic stack of images. The image stack was then processed through a Gaussian smoothing kernel with an SD of 0.5 to remove high-frequency spatial noise of the images. The SHG-lacking areas in the image stacks were then identified by comparing the image intensity to a pixel intensity threshold that was defined as 10% of the maximum image intensity. Contiguous regions with pixels below this intensity (with lowest 10% of signal range) were automatically masked as fluid-filled structures. Finally, the TPM signals and the extracted small structures were rendered together for 3D visualization by using FluoRender software (University of Utah Scientific Computing and Imaging Institute, Salt Lake City, UT, USA; www.sci.utah.edu/software/fluorender.html). A detailed description of the 3D segmentation techniques can be found in the supplementary material (Supplementary Methods S1).

Quantitative measurements of the main structure were performed based on original TPM images; a minimum of six measurements ($n = 6$) were taken at unique sites within the images collected from eight different eyes to calculate the mean and SD of the measured dimensions.

Histology

Selected eyes after TPM imaging were fixed in Davidson's Fixative (33% ethanol, 11% glacial acetic acid, 8% formaldehyde) overnight at 4° C, and then processed for paraffin embedding, sectioning (6-μm thick), and hematoxylin and eosin staining. Bright-field imaging of mouse histologic sections was performed with a Nikon Eclipse 80i microscope (Melville, NY, USA) equipped with a color camera (D5-Fi1; Nikon) using a ×20 CFI Plan Fluor objective (Nikon). Histologic measurements were performed using the NIS-Elements software package (Nikon).

Results

TPM Imaging of Intact Mouse Eyes

Figure 1 shows representative TPAF and SHG images of the AOS in unfixed enucleated C57BL/6 mouse eyes. Two-photon autofluorescence and SHG images were acquired transversely with the cornea oriented perpendicular to the objective lens. Figure 1A shows the "bird's eye" view of an entire mouse eye, a tiled image composed of 7 × 7 separately acquired TPM images. The size of the entire tiled image is 2.8 × 2.8 mm. The iris (IR) has strong TPAF (red) produced by melanin granules, whereas the cornea (CO) and the scleral tissue have strong SHG (blue) generated by its collagen components. Limbal regions from two different mouse eyes are shown at higher magnification in Figures 1B and 1C. As with our previous TPM imaging, we observed regions in each image that lacked both SHG emission and TPAF signal. A great many of these were small (with no single dimension <10 μm) and were excluded from further AOS segmentation analysis (Supplementary Methods S1).

Close to the corneal-scleral intersection were spaces absent of SHG signal assumed to be fluid filled. We tentatively identified the structures of the AOS through comparison with the histologic sections (Fig. 1D). The SC was largest of these fluid-filled spaces, identified by its relatively large size and its location near the anterior chamber at the insertion point of the IR and its relative location to the TM. Collector channels were visible as smaller open structures located within the scleral tissue and are connected to the SC. Aqueous veins were similarly sized fluid-filled structures located closer to the scleral surface. In some images, the TM could be identified as a thin strip of SHG signal immediately adjacent to SC (Fig. 1B). Figure 1D presents a hematoxylin and eosin–stained histologic section of a mouse eye with SC, TM, CO, and IR identified.

Figure 2 shows another image stack of spectral TPM images oriented in the transverse direction. The stack is centered at the depth of the SC in an intact C57BL/6 mouse eye. Figures 2A–C are transverse TPM images at three different depths (depth at 26, 28, and 30 μm from the scleral surface) around the SC. As described in the Methods, the images shown in Figure 2 were created by first pseudo-coloring each of the 32 spectral channels with a different color, and then combining the channels to create a full-color image. The collagen fibers of the CO generate strong SHG signal with a peak at 465 nm that is pseudo-colored "blue." The melanin of the ciliary body (CB) emits a broad fluorescent signal covering wavelengths from 490 to 690 nm. The combination of these multiple pseudo-colored emission channels appears "reddish" in the full-color image. Figure 2D is from the region noted in Figure 2A at higher magnification, constructed by adding the intensities of 25 SHG images separated by 1 μm. In this reconstruction, the area appears as an interwoven collagen assembly that due to its size and location is likely a septal bridge (SB). The SB also exhibits a weak TPAF, which could result from the collagen itself or may indicate the presence of elastin. These SBs connect the inner and outer wall of the SC located near the ostia of CC.[18,19]

Two-Photon Microscopy Imaging of Vascular-Perfused Eyes

To confirm the location and identity of specific distal AOS small structures among the large number of SHG-absent fluid-filled spaces in the TPM images, euthanized mice were cardiac perfused with 150 KDa FITC-labeled dextran to label the vascular structures. Z-stacked images were then scanned with a total depth of 46 μm with a step size of 1 μm. Figure 3 shows a representative z-stack scan of the AOS of an unfixed enucleated C57BL/6 mouse eye with FITC perfusion. Figure 3A is the sagittal view (x-z plane) of the image stack. Figures 3B–D are x-y plane images oriented perpendicular to the tissue surface at various depths. The depths (10, 24, and 38 μm) of the images are marked with solid lines in Figure 3A for clarity. In these

Investigative Ophthalmology & Visual Science

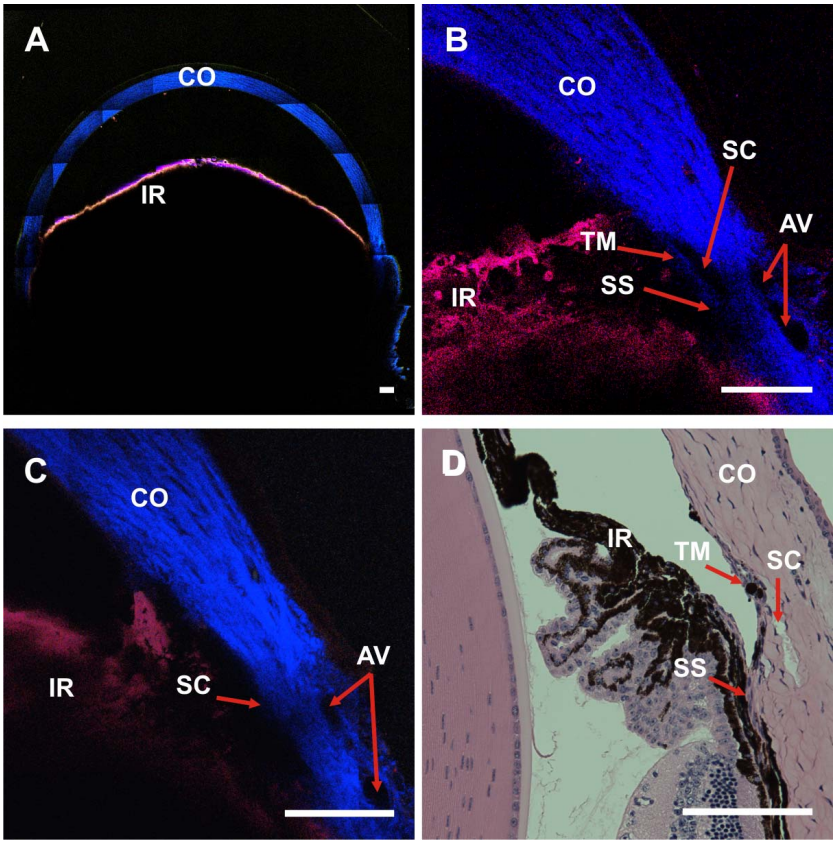

Figure 1. Spectral TPM of TPAF and SHG images of an unfixed, enucleated C57BL/6 mouse eye. (**A**) A TPM composite image tiled from a 7×7 image array shows the entire anterior cross-section (pixel size: 0.692 μm). *Red*: TPAF; *blue*: SHG. (**B**) and (**C**) are single TPM images of the limbal region from two different C57BL/6 mice (pixel size: 0.259 μm). The IR is visible by the TPAF signal (*red*) of the tissue melanin, and the collagen from the CO generates strong SHG (*blue*). Aqueous veins are identified by the absence of the SHG signal near the corneal/scleral junction. Schlemm's canal is identifiable as an area lacking SHG signal near the insertion point of the IR. The TM layer could be identified in (**B**) as a thin strip of faint SHG signal immediately adjacent to the SC. (**D**) A hematoxylin and eosin–stained histologic section of a C57Bl/6 eye. The relative locations of the SC, TM, and IR are in close proximity to those identified in the TPM images. SS, scleral spur. *Scale bar*: 100 μm.

images, the cardiac-perfused FITC-dextran labeled a few EVs (Fig. 3, arrowheads) in the superficial layers of scleral collagen. The vascular FITC-dextran fluorescence does not fill the entire region lacking SHG signal, suggesting that these vessels are lined with endothelial cells that are not visible using these TPM parameters. This dye had minimal but detectable penetration into a large number of other tube-like structures (arrows) that ran along the circumference of the eye, suggesting that during the time it took to image the perfused eyes some of the dye was able to diffuse backward into aqueous humor–filled structures (such as AV).

Using 3D data segmentation and rendering, the regions of the mouse sclera lacking SHG signal were processed to reveal the small internal structures of the AOS within the collagen tissue of the sclera. Images of these fluid-filled spaces were processed based on the segmentation and 3D rendering procedures described in the Methods section. The rendered 3D models were further dissected based on relative locations into regions representing SC, CC, and AV, and then these regions were pseudo-colored for clearer identification in Figures 4–6. Figures 4A and 4B are 3D rendered images from two different viewing angles using the same set of image data shown in Figure 3. Three-dimensional rendered animations showing the reconstructed tissue rotating along its principle axis are included in the supplemental information (Supplementary Movie S2). In these reconstructions, SC (light red), CC (green), and AV (yellow) were shown along with the SHG signal from the collagen located in the surrounding scleral tissue (transparent blue). The scale of the 3D-rendered images in the longitudinal direction was also dilated by a factor of two to improve visualization of these small structures within the collagen.

Labeling of vascular structures at the surface of the mouse limbus was very reproducible. All cardiac-perfused eyes ($n = 9$) showed staining of some circumferential vessels (EV) located at the limbus (Fig. 3, filled arrowheads), whereas other limbal vessels were consistently not filled with dye (Fig. 3, arrows). Figure 5 shows a 3D rendering and segmentation of an image stack collected at the limbus of one of the other C57BL/6 mouse eyes that was cardiac perfused with FITC-dextran. This reconstruction shows a large number of CCs connecting SC to the surface AVs and a single CC that connects at the junction of an aqueous-filled AV and an FITC-dextran–filled EV. Three-dimensional rendered animations showing the reconstructed tissue rotating along its principal axis are included in the supplemental information (Supplementary Movie S3).

Two-Photon Microscopy Imaging of Aqueous-Perfused Eyes

To confirm the location and identity of the proximal AOS structures by TPM imaging, 0.1 μm yellow fluorescent polystyrene beads were perfused through the cornea into the anterior chamber of enucleated mouse eyes. The fluorescence

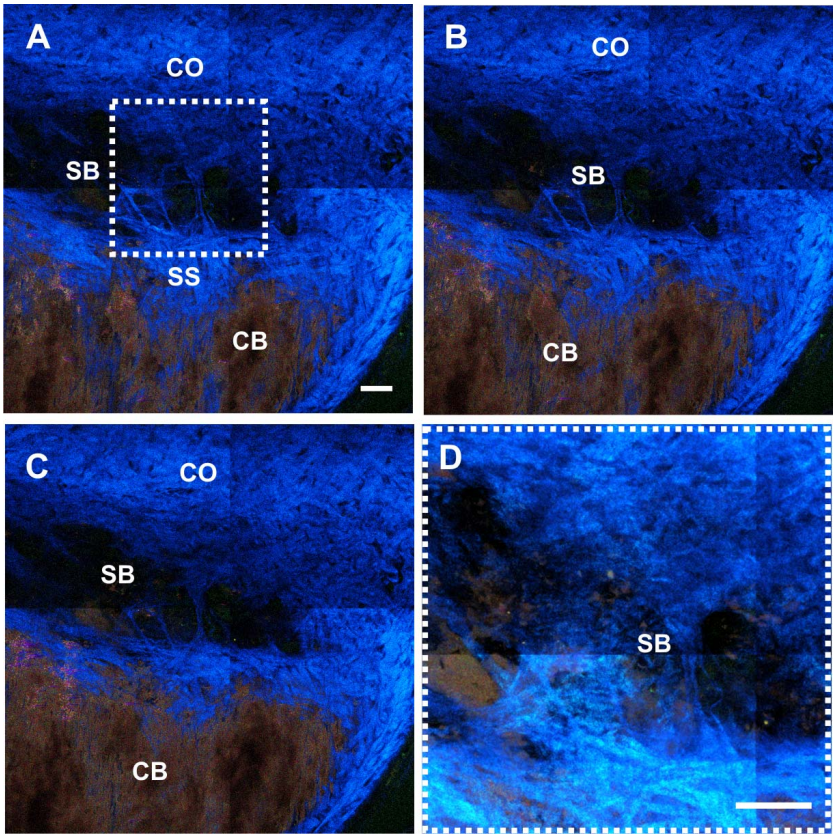

Figure 2. Spectral TPM images acquired at the SC in an enucleated C57BL/6 mouse eye. Second-harmonic generation signal within the SC reveals an interwoven collagen structure dividing the SC, potentially an SB. (**A–C**) Transverse images at various depths (at 26, 28, and 30 μm from the scleral surface, respectively) within the SC. (**D**) Intensity projection of 25 z-stack images separated by 1 μm revealed the SSs within the SC. *Scale bar*: 50 μm. *Pixel size*: 0.346 μm.

peak of the polystyrene beads was captured by a single channel of the Zeiss LSM 780 spectral detector that was distinct from the TPAF and SHG signal peaks. Figure 6 shows the 3D rendered and segmented reconstruction of the AOS. It is apparent from the reconstruction that the fluorescent beads were highly concentrated within the SC/TM at locations close to the entrances of the CCs. In addition, very few fluorescent beads penetrated into the SC and entered the distal structures of the AOS, indicating that fluorescent beads accumulate in the TM immediately adjacent to a SC. Three-dimensional rendered animations showing the reconstructed tissue rotating along its principal axis are included in the supplemental information (Supplementary Movie S4). Although 0.1-μm-sized beads are expected to penetrate farther into the AOS, high-resolution images of the polystyrene beads showed a high degree of clumping into large aggregates (data not shown).

Detailed segmentation of the AOS allowed for quantitative measurements of the SC, CC, and AV. The measurement results are tabulated in the Table. Each outcome was measured at six to eight different points (n = at least 6) selected from the raw image stacks of eight different C57BL/6 mouse eyes. The SC of C57BL/6 mouse eye forms an elliptical band around the limbus with average long and short axes measured to be 82.2 ± 22.2 μm and 6.7 ± 1.4 μm, respectively. These measurements are very close to measurements of SC taken from our histologic sections, which show major and minor axis lengths of 80.6 ± 23.1 μm and 9.0 ± 4.9 μm, respectively (n = 8 eyes). The diameter of the CC was found to vary across the entire length and was measured to be 25.6 ± 7.9 μm at the entrance (ostia) where it connects to the SC, dilating to 34.1 ± 13.1 μm at its midpoint, and finally narrowing to 18.3 ± 4.8 μm where it is connected with AVs. The length of the CC was measured to be 27.0 ± 2.9 μm. Figure 7 provides a schematic diagram indicating the detailed structures of the AOS and the symbols used in the Table.

Discussion

This study extends our previous work on AOS TPM imaging in ex vivo mouse eyes[16] using several improved techniques. Previous TPM imaging of the pigmented mouse eye using 800 nm excitation resulted in broad melanin autofluorescence[20] that could overwhelm the SHG and other autofluorescent signals, and therefore the intensity of the two-photon laser was kept low. In this work, the 930-nm excitation was effective in reducing autofluorescence from melanin granules while still yielding significant SHG signal from tissue collagen. Additionally, the longer excitation wavelengths resulted in a higher degree of optical penetration without a significant reduction in autofluorescent signal. Finally, the use of the 32-channel QUASAR spectral detector gives a spectral resolution of 8.9 nm per channel from 410 to 695 nm without the need of emission filters. The full-color multiphoton images of this study were created by first pseudo-coloring each of the 32 spectral channels a different color (ranging from dark blue to deep red). The advantage of analyzing data in this manner is that although various biomolecules/fluorophores may overlap spectrally, they can still be resolved in the rendered full-color images.

This work yielded high-resolution images of anatomical structures of a fresh, unfixed, and functional aqueous drainage

Investigative Ophthalmology & Visual Science

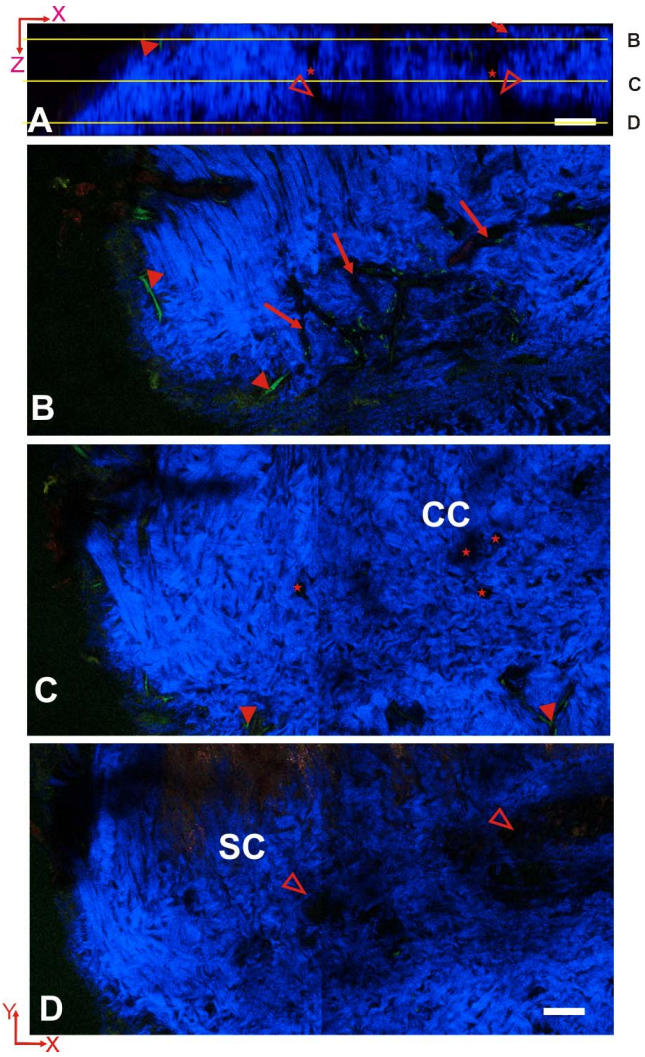

FIGURE 3. Spectral TPM image stack of the AOS acquired from an unfixed intact C57BL/6 mouse eye after cardiac perfused with 150 kDa FITC-dextran. (**A**) Sagittal view (x-z) of the AOS. The SHG-absent empty spaces constitute the AOS. Multiple CCs (*star*) connect between the SC (*hollow arrowhead*) and the outer AVs (*arrow*). (**B–D**) Transverse (x-y) images of the AOS at various depths (10, 24, and 38 μm) indicated by *lines* in (**A**). (**B**) At 10 μm below the scleral surface, AVs (*arrow*) form an interconnected network and EVs (*solid arrowhead*) were labeled by FITC-dextran (*green*). (**C**) At a depth of 24 μm, CCs (*star*) were visible as open structures within the scleral tissue (*blue*). (**D**) At a depth of 38 μm, the SC (*hollow arrowhead*) was evident as wide opened area lacking SHG (*blue*). *Scale bar*: 50 μm. *Pixel size*: 0.346 μm.

system. Casting models have shown that the AOS network is a part of an intricate drainage system and vasculature within the scleral tissue.[21–23] We attempted to reconstruct virtual castings of the AOS through segmentation analysis of the TPM image stacks. The image segmentation technique used here was based on (1) thresholding lower-intensity pixels from higher intensity pixels, (2) using the thresholding to identify AOS, and finally (3) drawing contours at the boundaries of the AOS. Three-dimensional models were created using these contours to identify various AOS fine structures based on their relative locations within the entire stack of images (described in detail in Supplementary Methods S1). Analysis of our 3D reconstructions demonstrated that our imaging method was able to detect all structures of the mouse AOS. Voids of different sizes and morphologies were noted in the SHG images of the scleral

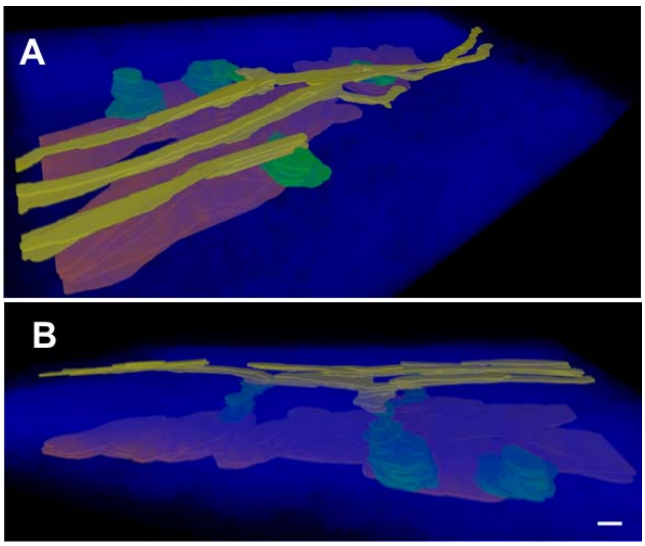

FIGURE 4. Three-dimensional image reconstruction and segmentation of the AOS taken from a spectral TPM image stack. The small structures within the AOS and their spatial relations can be visualized in this 3D reconstruction. (**A**) View from outside the eye looking into sclera and (**B**) the same reconstruction viewed from the side. SC (*red*), CCs (*green*), and AV (*yellow*), are rendered within the SHG collagen (*transparent blue*) within the scleral tissue. Note that one of CCs terminated within the sclera without connection to an AV. *Scale bar*: 30 μm in the *x*- and *y*-axes and 15 μm in the *z*-axis (the *z*-axis is dilated by a factor of 2 for better visualization).

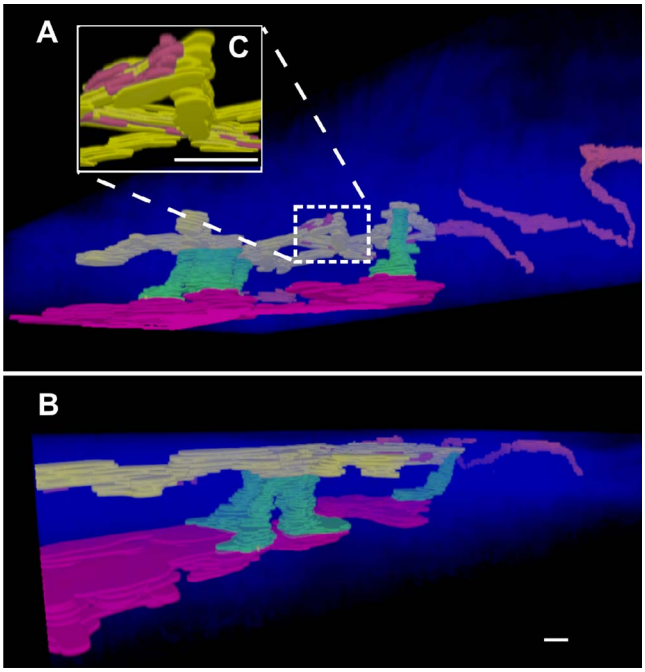

FIGURE 5. Three-dimensional reconstruction and segmentation of the AOS of a C57BL/6 mouse eye after cardiac perfusion with FITC-dextran. (**A**) View from inside the eye looking into sclera; (**B**) the same reconstruction viewed from the side. In this set of rendered images, multiple CCs (*green*) can be seen traveling radially from the SC (*red*) toward a pair of AVs (*yellow*). These AVs then terminate at EVs (*red/orange*), which then travel a convoluted path along the surface of the scleral collagen. In (**C**), the convoluted connection between AVs and EVs has been enlarged for better visualization. *Scale bar*: 30 μm in the *x*- and *y*-axes and 15 μm in the *z*-axis (the *z*-axis is dilated by a factor of 2).

Investigative Ophthalmology & Visual Science

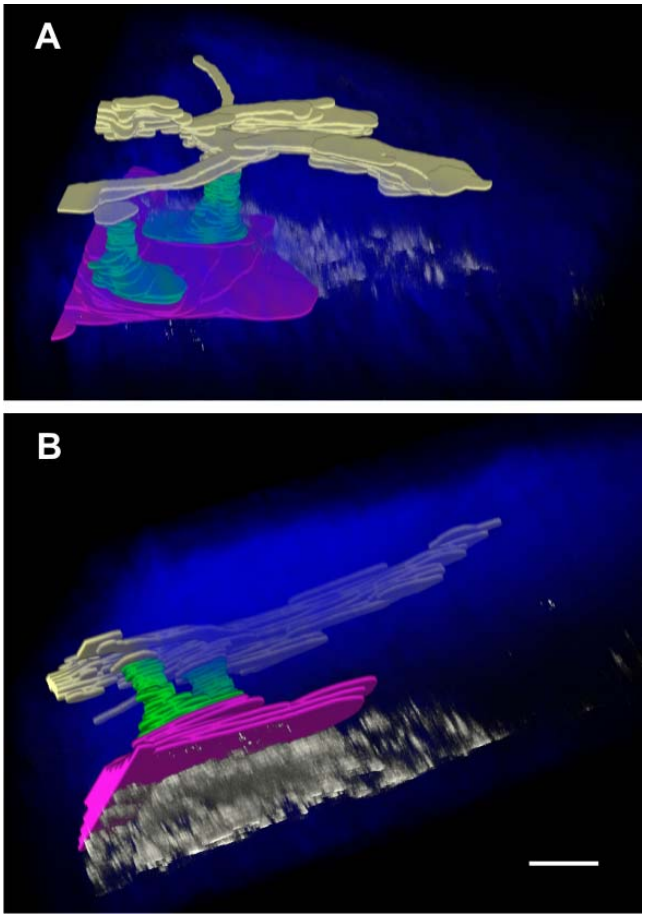

FIGURE 6. Three-dimensional image reconstruction and segmentation of the AOS of a C57BL/6 mouse eye perfused with 0.1 μm polystyrene beads through the cornea into the anterior chamber. (**A**) View from outside the eye looking into sclera, and (**B**) the same reconstruction viewed from the side. The fluorescent beads (*white*) accumulate beneath the SC (*red*) where the entrances of CCs (*green*) were located. There were a few fluorescent beads identified within the SC, CCs, and AVs (*yellow*). *Scale bar*: 30 μm in the *x*- and *y*-axes and 15 μm in the *z*-axis (the *z*-axis is dilated by a factor of 2).

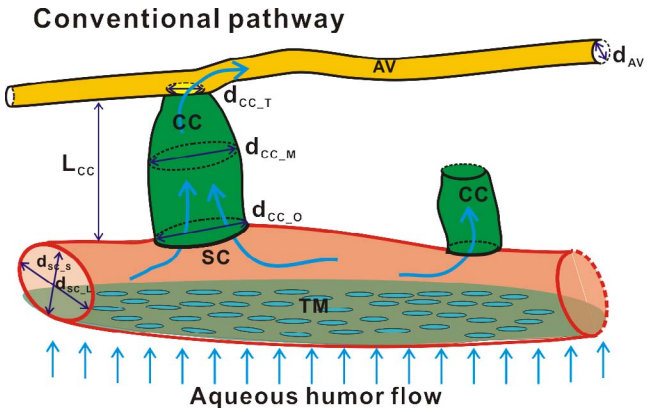

FIGURE 7. A schematic diagram illustrates the small structures (SC, CC, and AV) and the interconnections between these structures within the AOS. Dimensions of these small structures were quantitatively measured and tabulated in the Table: d_{SC_L} and d_{SC_S} indicate the long and short axes of SC; d_{CC_O}, d_{CC_M}, and d_{CC_T} represent the diameters of CC at the ostia, middle, and top locations; and the d_{AV}, represents the diameter of AV.

tissue. However, only large voids (>10 μm) that formed extended continuous connections were selected for further segmentation analysis of the structures of the AOS (described in Supplementary Methods S1). Future analysis of these smaller (<10 μm) regions could reveal the presence of nerves or other smaller lymphatics. However, in this work we focused only on those larger structures that were contiguous with the SC. The structures identified here correspond well to earlier work detailing the AOS system by standard histologic or electron microscopy methods. Three-dimensional reconstructions performed from our TMP images were qualitatively similar in all eight eyes imaged.

The collagen fibers of the mouse TM (<10-μm thick) could be detected in some but not all of our deep-tissue imaging (Fig. 1B). However, the nearby SC was much more readily detected, and used as a starting point for segmentation analysis. Three-dimensional tissue reconstructions of deep-tissue imaging revealed the elliptical SC. Occasionally, structures resembling SBs (Fig. 3D) that divided the SC were also detected. The elastic properties of these structures have been proposed to allow changes to SC shape and expansion of the juxtacanalicular region of SC under collector channels in response to higher pressure.[19,24,25] Connected to the SC were multiple small tube-like structures (CC) that extended radially from the interior of the eye toward the surface of the scleral tissue. These CCs had a wide range of diameters (~18–34 μm) and usually connected to a network of surface fluid-filled vessels (AVs; Fig. 3B), although in rare instances, a CC was detected that dead-ended within the sclera (Fig. 4B). This structure had an opening of 28.7 μm at the site of the SC, which is comparable to the size of other CC ostia (25.6 ± 7.9 μm, Table). However, this structure terminated after only 17 μm, whereas other CCs traveled on average 27.0 ± 2.9 μm to reach the AV. The large AVs imaged in this study travel circumferentially around the limbus until they eventually terminate at EVs, identified through by FITC-dextran cardiac perfusion (orange, Fig. 4B). The EV appeared as multiple branching structures throughout the collagen matrix of the sclera of the limbal region (Fig. 3B, arrowhead). The vascular dye had limited diffusion into the adjacent AV and was never detected within the CC (Fig. 3B, arrows). This indicated that although

TABLE. Measurements of SC, CC, and AV

	SC		CC				Lymphatic Vessel
	Long Axis, d_{SC_L}	Short Axis, d_{SC_S}	Diameter at Ostia, d_{CC_O}	Diameter at Midpoint, d_{CC_M}	Diameter at AV, d_{CC_T}	Long Axis, l_{CC}	Diameter, d_{AV}
Size, μm	82.2 ± 22.2	6.7 ± 1.4	25.6 ± 7.9	34.1 ± 13.1	18.3 ± 4.8	27.0 ± 2.9	12.5 ± 3.4

Data presented as the average ± SD of at least six measurements ($n = 6$) from TPM imaging of eight different C57BL/6 mouse eyes.

many vessels in the limbal region have similar size, shape, and location, we could distinguish between the aqueous humor and blood-containing vessels through the use of perfused dyes.

To characterize many of the components of the AOS, the sizes of SC, CC, and AV were measured from the TPM images in this study. Using our current imaging parameters, the thickness of the TM could be approximated from images like that shown in Figure 2. We are currently working on improving our imaging techniques to image the TM in high resolution and our preliminary results indicate that is possible. The SC of mouse eyes in this study, with its major axis length of 82.2 ± 22.2 μm and a minor axis length of 6.7 ± 1.4 μm, presented the same elliptical appearance as the human SC, although it was considerably smaller.[3,26,27] Our measurements of the orifice size of CCs range from 18.3 ± 4.8 μm to 34.1 ± 13.1 μm, which is comparable with previous descriptions.[8,28] Although the 3D models shown in Figures 4 to 6 were built on the acquired multiphoton images, the dimensions of the AOS fine structures reported in the article were actually measured directly from the raw multiphoton images. We did, however, repeat these measurements in the reconstructed 3D models and compared these measurements with the dimensions in the Table. The difference between the two measurements was less than 5% (data not shown); therefore, we conclude that the resolution of the 3D models approximates the resolution of the raw images. The rough appearance of the reconstructed 3D models is due to the Abbe's diffraction limit of the microscope objective, which demands that in multiphoton imaging the axial (z) resolution will be worse than the transverse (x and y) resolution.[29] In addition, although the use of 1 μm longitudinal step size reduced the experimental imaging time and kept the eye tissue fresh, the rough appearance can be improved by smaller step sizes (with increased imaging time). Finally, image segmentation that focuses on larger-diameter (>10 μm) channels that connect the SC and AV may potentially exclude aqueous outflow contributions from smaller channels that terminate elsewhere in the sclera. However, we reasonably assumed that these larger channels contribute most of the conventional aqueous fluid outflow. Future analysis of the high-resolution images obtained here could potentially allow investigation into the roles of these smaller channels.

Our past[14,30] and current TPM imaging corroborates and complements other in situ imaging work attempting to characterize the structures of the mouse AOS. Noninvasive imaging of mouse AOS has been performed using spectral-domain (SD)-OCT; however, only the SC was resolved for accurate size determination.[31] Truong et al.[32] also were able to image the SC in a live mouse transgenic for a fluorescent-protein marker for lymphatic endothelial cells. Using the same mouse, Gonzalez and Tan (*IOVS* 2013;54:ARVO E-Abstract 3550) were able to perform in vivo imaging of the distal AOS structures and the SHG of the scleral collagen using nonlinear microscopy. The SC, aqueous channels, and limbal vasculature were mapped in situ by confocal microscopy in fixed mouse corneo-scleral rims through the use of fluorescent antibody labeling.[33] More extensive work has been performed in imaging the human AOS system. Hann et al.[8] used 3D micro–computed tomography to identify the SC, CC, and episcleral vessels in an intact fixed human eye. Additionally, the advent of high-resolution SD-OCT has allowed the imaging of the entire AOS structures in enucleated perfused human.[34,35] Finally, Tan et al.[36] obtained high-resolution images of the cells within the fine collagen structures of the unfixed TM of recently harvested human corneo-scleral rims using nonlinear microscopic techniques similar to our own. Otherwise, to the best of our knowledge, this is the first report of the dimensions of SC, CC, and AV of unfixed, fresh enucleated C57BL/6 mouse eyes at micron-level resolution. The measurements presented are likely to be close to the true sizes of the AOS structures, as they are taken from fresh tissue that has not experienced the distortions caused by fixation or histologic processing.

The data presented here support the proposal that spectral TPM is well suited to help resolve the question of how the distal AOS structures contribute to IOP regulation or dysregulation. Early studies in perfused human eyes stripped of TM and outer wall of SC demonstrated that the distal AOS contributes approximately 25% to the total IOP.[37,38] This was verified in perfused eyes that had surgical or laser ablation of the outer wall of SC, a process that leaves the TM and inner wall of SC intact.[38,39] And although current theory holds that elevation of IOP in POAG is primarily due to changes in resistance of the inner wall of SC and juxtacanalicular region of the TM, there is some evidence that distal resistance to aqueous outflow is pressure sensitive, with increased perfusion pressure leading to increased distal resistance.[40] Other distal structures that are potential imaging targets are the CC ostia, which are hypothesized to allow preferential flow within localized regions of SC.[41,42] These ostia appear to respond to changes in IOP, because high-resolution SD-OCT imaging has shown that CC ostia dilate with increases in static pressure (Lei, et al. *IOVS* 2015;56:ARVO E-Abstract 3258). Additionally, spectral TPM is a novel platform for future drug studies, as this imaging modality has the unique ability to determine how new therapeutic agents influence the distal AOS. Imaging the AV and EV may be particularly relevant for evaluating the class of IOP-lowering drugs, the rho-kinase (ROCK) inhibitors, that reportedly can influence both arteriole and epi-scleral venous pressure.[43,44] In conclusion, we propose that developing spectral TPM for in vivo imaging has great potential for the clinical diagnoses of POAG. The ability to precisely measure proximal AOS structures linked to POAG development (such as SC) is extremely relevant for clinical diagnosis. Additionally, the potential ability of spectral TPM to assess the function of distal AOS (CC and AV) structures may also assist clinical therapies for POAG that seek to bypass a dysfunctional TM and SC.

Acknowledgments

Supported by National Institutes of Health (NIH) Grant 1K25DK095232-01A1(TCL), Macau Science and Technology Department Fund Grant 087/2012/A3 (PUM, TCL, SHP, and MIV), and the China Scholarship Council (XZ, NL). The University of Colorado Anschutz Medical Campus Advanced Light Microscopy Core is supported in part by NIH/National Center for Advancing Translational Sciences Colorado Clinical and Translational Sciences Institute Grant UL1 TR001082.

Disclosure: **X. Zhang**, None; **N. Liu**, None; **P.U. Mak**, None; **S.H. Pun**, None; **M.I. Vai**, None; **O. Masihzadeh**, P; **M.Y. Kahook**, P; **T.C. Lei**, P; **D.A. Ammar**, P

References

1. Johnson M. What controls aqueous humour outflow resistance? *Exp Eye Res*. 2006;82:545–557.
2. Kagemann L, Wollstein G, Ishikawa H, et al. Identification and assessment of Schlemm's canal by spectral-domain optical coherence tomography. *Invest Ophthalmol Vis Sci*. 2010;51:4054–4059.
3. Usui T, Tomidokoro A, Mishima K, et al. Identification of Schlemm's canal and its surrounding tissues by anterior segment Fourier domain optical coherence tomography. *Invest Ophthalmol Vis Sci*. 2011;52:6934–6939.
4. Dada T, Gadia R, Sharma A, et al. Ultrasound biomicroscopy in glaucoma. *Surv Ophthalmol*. 2011;56:433–450.
5. Dusak A, Baykara M, Ozkaya G, Erdogan C, Ozcetin H, Tuncel E. Ultrasound biomicroscopic evaluation of anterior segment

cysts as a risk factor for ocular hypertension and closure angle glaucoma. *Int J Ophthalmol*. 2013;6:515–520.

6. Grulkowski I, Liu JJ, Potsaid B, et al. Retinal, anterior segment and full eye imaging using ultrahigh speed swept source OCT with vertical-cavity surface emitting lasers. *Biomed Opt Express*. 2012;3:2733–2751.
7. Leung CK, Weinreb RN. Anterior chamber angle imaging with optical coherence tomography. *Eye*. 2011;25:261–267.
8. Hann CR, Bentley MD, Vercnocke A, Ritman EL, Fautsch MP. Imaging the aqueous humor outflow pathway in human eyes by three-dimensional micro-computed tomography (3D micro-CT). *Exp Eye Res*. 2011;92:104–111.
9. Gibson EA, Masihzadeh O, Lei TC, Ammar DA, Kahook MY. Multiphoton microscopy for ophthalmic imaging. *J Ophthalmol*. 2011;2011:870879.
10. Piston DW. Imaging living cells and tissues by two-photon excitation microscopy. *Trends Cell Biol*. 1999;9:66–69.
11. Benninger RK, Piston DW. Two-photon excitation microscopy for the study of living cells and tissues. *Curr Protoc Cell Biol*. 2013;Chapter 4:Unit 4.11.11–24.
12. Campagnola P. Second harmonic generation imaging microscopy: applications to diseases diagnostics. *Anal Chem*. 2011; 83:3224–3231.
13. Ammar DA, Lei TC, Gibson EA, Kahook MY. Two-photon imaging of the trabecular meshwork. *Mol Vis*. 2010;16:935–944.
14. Johnson AW, Ammar DA, Kahook MY. Two-photon imaging of the mouse eye. *Invest Ophthalmol Vis Sci*. 2011;52:4098–4105.
15. Masihzadeh O, Lei TC, Ammar DA, Kahook MY, Gibson EA. A multiphoton microscope platform for imaging the mouse eye. *Mol Vis*. 2012;18:1840–1848.
16. Masihzadeh O, Ammar DA, Kahook MY, Gibson EA, Lei TC. Direct trabecular meshwork imaging in porcine eyes through multiphoton gonioscopy. *J Biomed Opt*. 2013;18:036009.
17. Delori FC, Webb RH, Sliney DH. Maximum permissible exposures for ocular safety (ANSI 2000), with emphasis on ophthalmic devices. *J Opt Soc Am A Opt Image Sci Vis*. 2007; 24:1250–1265.
18. Spencer WH. Symposium: microsurgery of the outflow channels. Histologic evaluation of microsurgical glaucoma techniques. *Trans Am Acad Ophthalmol Otolaryngol*. 1972; 76:389–397.
19. Hann CR, Vercnocke AJ, Bentley MD, Jorgensen SM, Fautsch MP. Anatomic changes in Schlemm's canal and collector channels in normal and primary open-angle glaucoma eyes using low and high perfusion pressures. *Invest Ophthalmol Vis Sci*. 2014;55:5834–5841.
20. Teuchner K, Ehlert J, Freyer W, et al. Fluorescence studies of melanin by stepwise two-photon femtosecond laser excitation. *J Fluoresc*. 2000;10:275–281.
21. Ashton N. Anatomical study of Schlemm's canal and aqueous veins by means of neoprene casts. Part I. Aqueous veins. *Br J Ophthalmol*. 1951;35:291–303.
22. Ashton N. Anatomical study of Schlemm's canal and aqueous veins by means of neoprene casts. II. Aqueous veins. *Br J Ophthalmol*. 1952;36:265–267.
23. Van Buskirk EM. The canine eye: the vessels of aqueous drainage. *Invest Ophthalmol Vis Sci*. 1979;18:223–230.
24. Johnson DH. Histologic findings after argon laser trabeculoplasty in glaucomatous eyes. *Exp Eye Res*. 2007;85:557–562.
25. Hann CR, Fautsch MP. The elastin fiber system between and adjacent to collector channels in the human juxtacanalicular tissue. *Invest Ophthalmol Vis Sci*. 2011;52:45–50.
26. Allingham RR, de Kater AW, Ethier CR. Schlemm's canal and primary open angle glaucoma: correlation between Schlemm's canal dimensions and outflow facility. *Exp Eye Res*. 1996;62: 101–109.
27. Irshad FA, Mayfield MS, Zurakowski D, Ayyala RS. Variation in Schlemm's canal diameter and location by ultrasound biomicroscopy. *Ophthalmology*. 2010;117:916–920.
28. Gong H, Francis A. Schlemm's canal and collector channels as therapeutic targets. In: Samples JR, Ahmed IIK eds. *Surgical Innovations in Glaucoma*. New York, NY: Springer-Verlag; 2014:3–25.
29. Tsai PS, Kleinfeld D. In vivo two-photon laser scanning microscopy with concurrent plasma-mediated ablation principles and hardware realization. In: Frostig RD, ed. *In Vivo Optical Imaging of Brain Function*. Boca Raton, FL: CRC Press; 2009:59-116. Available at: http://www.ncbi.nlm.nih.gov/books/NBK20231/. Accessed October 6, 2015.
30. Ammar DA, Lei TC, Masihzadeh O, Gibson EA, Kahook MY. Trans-scleral imaging of the human trabecular meshwork by two-photon microscopy. *Mol Vis*. 2011;17:583–590.
31. Li G, Farsiu S, Chiu SJ, et al. Pilocarpine-induced dilation of Schlemm's canal and prevention of lumen collapse at elevated intraocular pressures in living mice visualized by OCT. *Invest Ophthalmol Vis Sci*. 2014;55:3737–3746.
32. Truong TN, Li H, Hong YK, Chen L. Novel characterization and live imaging of Schlemm's canal expressing Prox-1. *PLoS One*. 2014;9:e98245.
33. van der Merwe EL, Kidson SH. The three-dimensional organisation of the post-trabecular aqueous outflow pathway and limbal vasculature in the mouse. *Exp Eye Res*. 2014;125: 226–235.
34. Hariri S, Johnstone M, Jiang Y, et al. Platform to investigate aqueous outflow system structure and pressure-dependent motion using high-resolution spectral domain optical coherence tomography. *J Biomed Opt*. 2014;19:106013.
35. Francis AW, Kagemann L, Wollstein G, et al. Morphometric analysis of aqueous humor outflow structures with spectral-domain optical coherence tomography. *Invest Ophthalmol Vis Sci*. 2012;53:5198–5207.
36. Tan JC, Gonzalez JM Jr, Hamm-Alvarez S, Song J. In situ autofluorescence visualization of human trabecular meshwork structure. *Invest Ophthalmol Vis Sci*. 2012;53:2080–2088.
37. Grant WM. Experimental aqueous perfusion in enucleated human eyes. *Arch Ophthalmol*. 1963;69:783–801.
38. Ellingsen BA, Grant WM. Trabeculotomy and sinusotomy in enucleated human eyes. *Invest Ophthalmol Vis Sci*. 1972;11: 21–28.
39. Schuman JS, Chang W, Wang N, de Kater AW, Allingham RR. Excimer laser effects on outflow facility and outflow pathway morphology. *Invest Ophthalmol Vis Sci*. 1999;40:1676–1680.
40. Rosenquist R, Epstein D, Melamed S, Johnson M, Grant WM. Outflow resistance of enucleated human eyes at two different perfusion pressures and different extents of trabeculotomy. *Curr Eye Res*. 1989;8:1233–1240.
41. Battista SA, Lu Z, Hofmann S, Freddo T, Overby DR, Gong H. Reduction of the available area for aqueous humor outflow and increase in meshwork herniations into collector channels following acute IOP elevation in bovine eyes. *Invest Ophthalmol Vis Sci*. 2008;49:5346–5352.
42. Hann CR, Fautsch MP. Preferential fluid flow in the human trabecular meshwork near collector channels. *Invest Ophthalmol Vis Sci*. 2009;50:1692–1697.
43. Kiel JW, Kopczynski CC. Effect of AR-13324 on episcleral venous pressure in Dutch belted rabbits. *J Ocul Pharmacol Ther*. 2015;31:146–151.
44. Hein TW, Rosa RH Jr, Yuan Z, Roberts E, Kuo L. Divergent roles of nitric oxide and rho kinase in vasomotor regulation of human retinal arterioles. *Invest Ophthalmol Vis Sci*. 2010;51: 1583–1590.

Investigative Ophthalmology & Visual Science